JGR Oceans

RESEARCH ARTICLE
10.1029/2018JC014844

Revised Global Wave Number Spectra From Recent Altimeter Observations

Oscar Vergara[1], Rosemary Morrow[1], Isabelle Pujol[2], Gérald Dibarboure[3], and Clément Ubelmann[2]

[1]LEGOS, IRD/CNES/CNRS/University of Toulouse, Toulouse, France, [2]CLS Space Oceanography, Toulouse, France, [3]CNES, Toulouse, France

Key Points:
- Sea surface height spectral slopes in the mesoscale wavelength range are consistent with theoretical considerations in the extratropics
- Spectral slopes in the tropics are close to k-2, likely related to the Internal Gravity Wave field
- Spectral slopes in the mesoscale wavelength range vary seasonally as shown by ocean simulations, due to the seasonality of local dynamics

Correspondence to:
O. Vergara,
oscar.vergara@legos.obs-mip.fr

Citation:
Vergara, O., Morrow, R., Pujol, I., Dibarboure, G., & Ubelmann, C. (2019). Revised global wave number spectra from recent altimeter observations. *Journal of Geophysical Research: Oceans*, *124*, 3523–3537. https://doi.org/10.1029/2018JC014844

Received 5 DEC 2018
Accepted 23 APR 2019
Accepted article online 30 APR 2019
Published online 4 JUN 2019

Abstract Global sea surface height wave number spectra are revisited using the most recent, lower-noise satellite altimeter missions from Saral/AltiKa and Sentinel-3 and compared to Jason-2 wave number spectra. Spectral preprocessing is configured to minimize the spectral slope distortion in the mesoscale wavelength range. A geographically variable wavelength range is used to calculate the spectral slopes, taking into account the regional eddy length scales based on the local Rossby radius. This dynamical wavelength range increases the spectral slope by 0.5 in middle to high latitudes, compared to a fixed wavelength range, and by -1.0 to 1.0 in different regions of the intertropical band. Using this dynamical wavelength range, mean sea surface height wave number spectra for these lower-noise missions exhibit low slope values (k^{-2}) in the intertropical band, values of $k^{-11/3}$ in the midlatitudes, and reaches k^{-5} in the subpolar regions and the Antarctic circumpolar current. An important seasonality is also revealed, with mesoscale spectral slope amplitudes decreasing in winter by 0.5 to 1.5 compared to summer, for the middle- to high-energy regions. A phase-locked internal tide correction is tested but has only a small impact on the spectral slope estimates when using the dynamical wavelength range.

1. Introduction

Satellite altimetry provides a unique observation of a wide range of ocean scales with its fine along-track resolution and its global and long-term coverage. This global coverage allows us to determine both the horizontal wave number and frequency spectra (Wortham & Wunsch, 2013). Global sea surface height (SSH) wave number spectra have been calculated from along-track satellite altimetry since the days of Seasat in the early 1980s (Fu, 1983) and continued with Geosat (Le Traon et al., 1990), Topex-Poseidon (Stammer, 1997), and more recently with Jason-class observations (Le Traon et al., 2008; Xu & Fu, 2012).

The slope of the altimetric SSH wave number spectrum over the mesoscale wavelength band has been used to infer the processes that govern the energy exchanges in quasi-geostrophic (QG) oceanic flows (Charney, 1971), which also involve subsurface ocean dynamics. Observed Jason-1 SSH spectral slopes over the fixed mesoscale band from 70 to 250 km wavelength are generally shallower than the QG theory predictions of k^{-5} (Xu & Fu, 2012). On the other hand, Le Traon et al. (2008) showed that the SSH wave number spectral slope is closer to the prediction of the theory of surface quasi-geostrophic (SQG) turbulence (Blumen, 1978; Held et al., 1995) in the high-energy midlatitude regions, which is related to the impact of density changes near the surface boundary, yielding a spectral slope in SSH around $k^{-11/3}$. This was also confirmed subsequent studies (e.g., Dufau et al., 2016; Hosoda et al., 2015; Xu & Fu, 2012).

The global distribution of SSH spectral slope has revealed a strong geographical dependence (Dufau et al., 2016; Xu & Fu, 2012; Zhou et al., 2015), with low values ($k^{-1.5} - k^{-2}$) in the intertropical band (20°S–20°N) and in low-energy eastern boundary regions, and progressively steeper slopes toward higher latitudes, reaching $k^{-11/3}$ in the highly energetic regions. These low SSH spectral slopes have been attributed to the presence of internal gravity waves (IGWs) from atmospheric or tidal forcing that can dominate the SSH in regions of low eddy energy, as shown in simulations (Richman et al., 2012; Savage, Arbic, Alford, et al., 2017; Tchilibou et al., 2018) and in altimetric observations (Dufau et al., 2016; Rocha, Gille, et al., 2016). Indeed, the unresolved internal tides lead to peaks in spectral energy around 100-200 km wavelength band, depending on the region, that can even lead to positive spectral slope estimates in low eddy energy regions (Dufau et al., 2016). Qiu et al. (2018) recently investigated the geographical distribution of the IGW field with the MITGCM model, which is characterized by a k^{-2} kinetic energy (KE) and SSH wave number spectral slope

(Garrett & Munk, 1972), and quantified regionally the scales of motion impacted by these high-frequency waves.

High-resolution modeling studies have also suggested an important seasonal cycle in the variability of the mesoscale to submesoscale wavelength range, affecting the SSH wave number spectral slope (e.g., Brannigan et al., 2015; Qiu et al., 2018; Sasaki et al., 2014). During winter-spring, energetic mixed-layer instabilities can develop in the deeper surface mixed layers adding more submesoscale energy, and model simulations reveal flatter KE spectral slopes in the midlatitudes, close to -2 (-4 in SSH) in winter compared to the steeper -3 (-5 in SSH) slopes in summer (Sasaki et al., 2014). Such seasonal variability has also been diagnosed from altimetry observations (Dufau et al., 2016; Morrow et al., 2017; Qiu et al., 2014) and from in situ observations (Callies et al., 2015). The mixture of winter and summer observations may contribute to the annual mean SSH spectral slopes in the range of -4 and -4.5 in the high eddy-energy regions (e.g., Xu & Fu, 2012), where the seasonal cycle is strong.

Given the important geographical variations, the seasonal variability in the slopes, and the dominance of IGWs in some geographical regions, interpreting these altimetric SSH slopes in terms of theoretical QG or SQG energy cascades needs to be carefully made. In addition, the methodology used to calculate the global SSH spectra can impact the spectral slope estimates. Much attention has been given to the techniques that reduce the altimetric instrument noise in the spectral estimates, since it impacts directly on the restitution of the smaller wavelengths. Unbiasing the altimetric wave number spectra by removing a fixed-value noise floor is often applied (e.g., Dufau et al., 2016; Xu & Fu, 2012) to improve the spectral slope estimates at small wavelengths (less than 100 km). Even so, the Jason-class satellites can generally only resolve scales down to ~70-km wavelength, Saral/AltiKa and Sentinel-3 down to 35-50 km (Raynal et al., 2017), and this limits our observations of the smaller mesoscale energy cascade in regions with small Rossby radii (e.g., high latitudes, Mediterranean Sea, and coastal regions).

Additionally, global wave number spectral slopes have often been calculated over a fixed wavelength range from 70 to 250 km, which is assumed to be characteristic of mesoscale variability (Dufau et al., 2016; Le Traon et al., 2008; Xu & Fu, 2011). This may be well adapted to the midlatitudes but poorly frames the steepest slopes in the tropics and high latitudes (Dufau et al., 2016). Spectral processing techniques also play a role in modifying the spectral slope, and recently, Tchilibou et al. (2018) highlighted that short segment lengths and certain windowing choices for the spectral estimates can contribute to reducing the SSH wave number spectral slopes in the tropics.

Here we revisit the methodology used to compute the global SSH wave number spectral slopes, by (1) exploring the more recent altimetric missions with their lower noise level, using 2 years of Saral/AltiKa data and 9 months of the Sentinel-3 global Synthetic Aperture Radar (SAR) altimetric data, as well as 5 years of Jason-2 data. This should improve the restitution of the spectral slopes at high latitudes, where the steepest energy cascade occurs at shorter wavelengths. (2) We will also use a geographically variable "mesoscale" wavelength range to compute the spectral slopes, taking into account the geographical dependence of the characteristic eddy length scales based on their local Rossby radius, following Eden (2007). (3) We choose spectral preprocessing techniques that minimize the spectral slope modification, with particular care taken in the tropics, following from the work of Tchilibou et al. (2018). (4) We will test the impact of the phase-locked internal tide on our estimates of SSH wave number spectral slopes by applying a recently developed phase-locked internal tide correction (Zaron & Ray, 2017) that reduces the main internal tide SSH power peaks.

2. Data and Methods

2.1. SSH data

Along-track SSH data from three different missions (Jason-2, SARAL/AltiKa, and Sentinel-3A) are analyzed at a global scale over two different time periods, spanning from 2013 to 2017. The first period analyzed covers from March 2013 to March 2015, which corresponds to the time period where altimetric time series from Jason-2 and AltiKa overlap. Starting from June 2016, SARAL/AltiKa mission is no longer on a repetitive orbit due to technical issues in the onboard momentum wheels first reported at the end of March 2015, which dictated our choice for the period of comparison between AltiKa and Jason-2. The second period

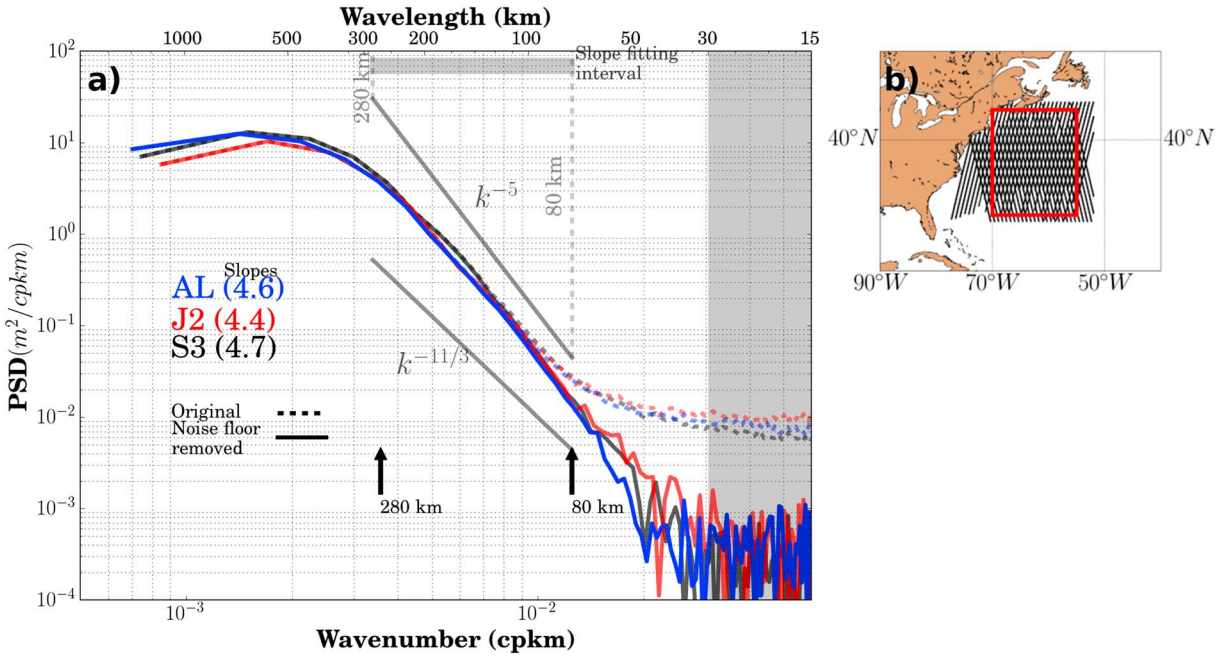

Figure 1. (a) Unbiased (full line) and original (dashed line) mean spectrum for AltiKA (AL), Jason-2 (J2), and Sentinel-3A (S3), inside the (b) Gulf Stream region. Spectral slopes computed inside the local wavelength range 80-280 km are indicated in parentheses. Gray area in (a) corresponds to the wavelength interval 15-30 km, where the noise level is computed (this region is therefore not interpretable). Spectral slopes corresponding to k^{-5} and $k^{-11/3}$ are also indicated. Black arrows and gray band denote the limits of the wavelength range used to compute the spectral slope. PSD = power spectral density.

analyzed spans from December 2016 to October 2017, which is the common period for the SARAL/AltiKa (SARAL/AltiKa-Drifting Orbit) and Sentinel-3A data sets.

Along-track SSH observations are maintained at their original observational position and are corrected for all instrumental, environmental, and geophysical corrections. Only time dependent variations of SSH are considered, following Stammer (1997), Le Traon et al. (2008), and Xu and Fu (2011, 2012). Sea level anomalies are computed for all missions by subtracting the Mean Sea Surface Model CNES_CLS_2015 (Pujol et al., 2018; Schaeffer et al., 2016) from the along-track SSH measurements. The Mean Sea Surface Model data used can be found in the AVISO (https://www.aviso.altimetry.fr).

Jason-2 (J2) is a conventional pulse-width limited altimeter operating in the Ku-band (Lambin et al., 2010) and was the reference mission for the altimetry constellation, followed by Jason-3 after its launch in early 2016. SARAL/AltiKa (AL), with its 40-Hz Ka-band emitting frequency, its wider bandwidth, lower orbit, increased pulse repetition, and reduced antenna beam width, provides a smaller footprint with a lower noise level than Ku-band altimeters (Verron et al., 2015). On the other hand, the recently launched Sentinel-3A (S3) altimeter differs from the J2 and AL in that it embarks a dual-frequency (Ku and C-band) SAR altimeter, with an along-track posting of 300 m in SAR mode (20 Hz), which provides useful sea level observations near coastal areas where topographic features often pollute the footprint of conventional altimeters (Andersen et al., 2016; Cotton et al., 2016). For all three missions, we analyze the 1-Hz data only, which for both J2 and AL has a flat (white) noise floor, whereas the noise floor at 1 Hz has a slope (red) for S3.

2.2. Unbiased Wave Number Spectral Estimates

We compute the SSH anomaly wave number power spectral density (PSD) for each mission following the methodology developed in Dufau et al. (2016). The along-track measurements are subsampled inside a 15° × 15° box. Segments of constant length (1,500 km) are selected, to ensure adequate coverage in the tropics following Tchilibou et al. (2018). These segment lengths are longer than those used by Dufau et al. (2016) of 560 km and Xu and Fu (2012) of 1,000 km. Individual wave number spectra are estimated on each pass for each segment and then averaged, yielding the average spectrum inside the square box (Figure 1).

The spectral estimates are obtained by applying a fast Fourier transform to the along-track SSH anomaly data. A Tukey window of 0.5 width is applied to the data (Tchilibou et al., 2018) in order to minimize boundary effects. When performing the fast Fourier transform analysis, spatial overlapping of the along-track samples is applied but limited to a 250 km (or even less in some regions). This increases the statistical confidence of the spectral estimates.

In order to avoid an artificial overrepresentation of certain spatial scales introduced by the overlapping, we verified that the spatial scale of the overlapping is larger than the local spatial decorrelation scale.

This process is repeated adding an offset in the zonal and meridional direction (2° in our case), in order to cover the global ocean. For each average spectrum, we estimate the 1-Hz error level by fitting a straight line to the sea level anomaly PSD for wavelength smaller than 30 km. We fit a horizontal line in the case of AL and J2, and an inclined straight line for S3 due to its characteristic red noise (Raynal et al., 2017). The geographical and seasonal characteristics of this noise are discussed in section 3.1. The noise level obtained by this fitting method is then substracted from the PSD estimates over the entire wave number range, which gives an unbiased estimation of the spectral slope over the mesoscale range (see Appendix A for details). The results are then presented on a 2° × 2° global grid (which implies an overlapping of ~87% between adjacent cells).

2.3. Variable Wavelength Range Technique

We estimate the spectral slope for each average spectrum (after removing the noise level), by least squares fitting a straight line inside a wavelength range defined individually for each 15° × 15° box. In contrast to previous studies, we chose to use a variable mesoscale wavelength range for each location. This choice derives from the fact that mesoscale characteristics are not constant across the global ocean and particularly they exhibit important meridional variations in size (Jacobs et al., 2001). To tackle this issue, we use the eddy length scale introduced by Eden (2007) as a proxy for the local characteristic mesoscale wavelength (described in Appendix A), which defines the lower wavelength limit for the mesoscale slope fitting range in the spectrum. The upper wavelength limit is defined by the change of slope itself (right and left black arrows at the bottom of Figure 1). Further details and evaluation of the technique are given in Appendix A.

The benefit of using a variable mesoscale wavelength range to fit the spectral slope is illustrated in Figure 2. Dufau et al. (2016) had suggested that using a fixed 70- to 250-km wavelength range may result in an underestimation of the spectral slopes in the tropics and high latitudes, since the mesoscale energy cascade occurs at longer or shorter wavelengths, respectively. In these regions we do observe an increased spectral slope estimate using our variable mesoscale range. In contrast, in the midlatitudes the spectral slopes are slightly decreased compared to the fixed wavelength range. We illustrate in Figure 2c several cases where the differences in spectral slope estimates are important. In particular, we observe that the higher spectral slope values obtained in the Eastern Tropical Pacific (Figure 2c, box 2) are related to the impact of the internal tide signature in the fixed wavelength spectral estimate (note that the energy increase around 100-km wavelength is inside the 70- to 250-km band but outside the variable wavelength range of 100-500 km here). Using a variable wavelength range to fit the spectral slope that takes into account local stratification and Rossby number allows us to better identify the wavelength range where the cascade of geostrophically balanced motions is present.

We also find regions where our methodology yields smaller spectral slope values, as opposed to the case when a fixed wavelength range is used (e.g., midlatitudes in the central Pacific [Figure 2c, box 1] western tropical Pacific, and eastern tropical Atlantic). The shape of the SSH signal in the 70- to 250-km wavelength range for these regions shows a bump around 180-km wavelength, typical of unbalanced internal tide motions. For this box, the bump occurs in the lower end of our "mesoscale" range and flattens our spectral slopes, whereas it impacts the higher end of the fixed wavelength range, artificially increasing that slope estimate. Our variable wavelength methodology generally has a larger wavelength range in these zones (see Appendix A and Figure 2c, box 1), which mostly minimizes this effect.

In the following section, we will examine in detail how the slope values vary compared to the theoretically predicted ones.

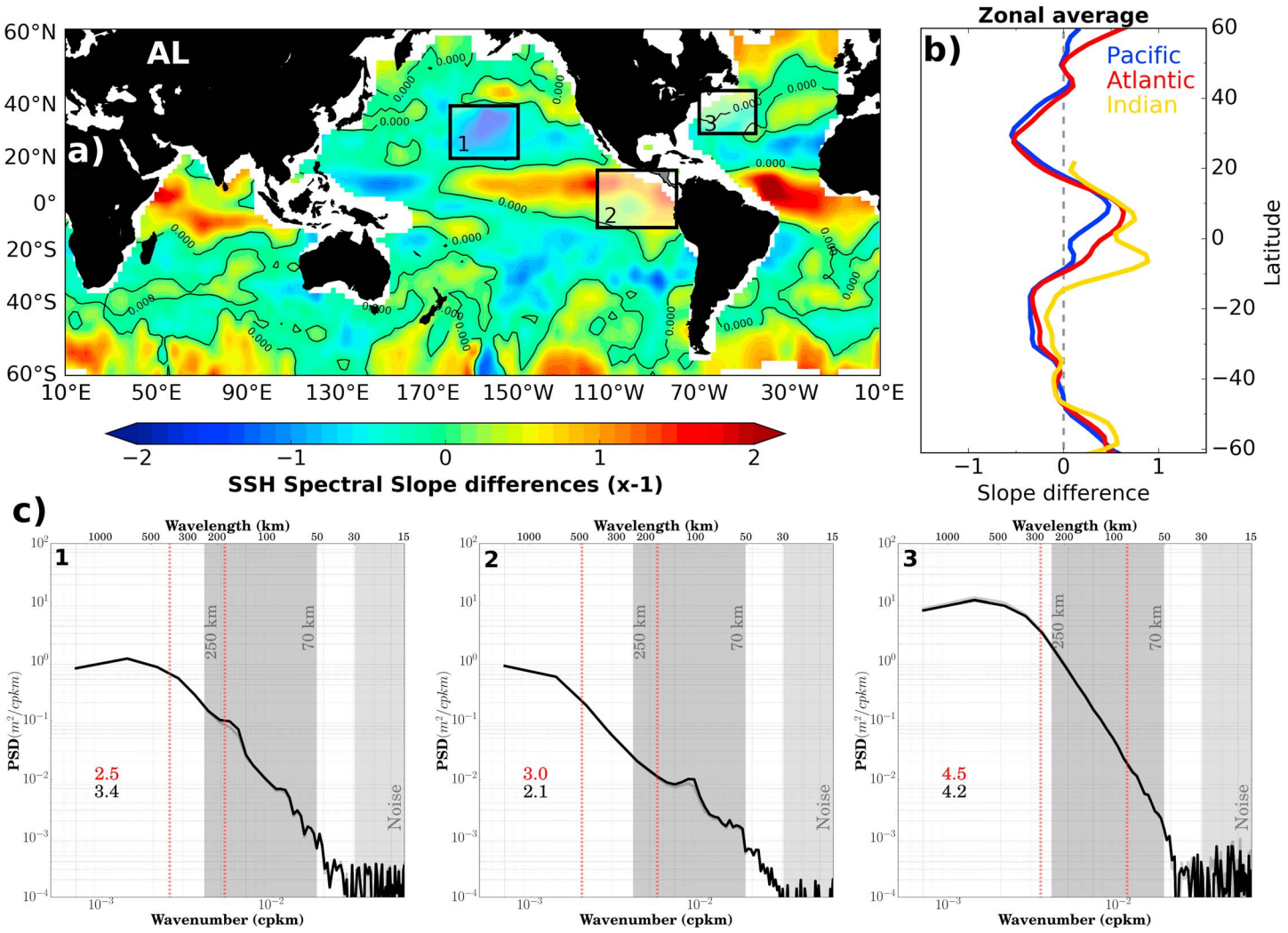

Figure 2. (a) Difference between the spectral slope estimations using a fixed wavelength range and the current approach (variable wavelength range), for the global ocean using AltiKa SSH anomalies. (b) Zonal average of the values presented in (a) for different ocean basins. Using a variable spectral range fits steeper slopes in the midlatitudes and in the intertropical Indian, Atlantic, and Eastern Pacific Oceans. (c) Wave number spectral estimates averaged inside the square regions depicted in (a). Different wavelength ranges are also represented in (c): variable wavelength range used to fit the spectral slopes (red dashed lines), fixed wavelength range (70-250 km; dark gray shading), and wavelength range used to compute the white noise level (15-30 km; light gray shading). Spectral slope values computed inside the variable wavelength range (red) and fixed wavelength range (black) are also indicated. Spectral estimates obtained after applying the correction for phase-locked internal tides are also included (gray line). SSH = sea surface height; PSD = power spectral density.

3. Global Spectral Slope in the Mesoscale Wavelength Range

3.1. Altimeter SSH Error Levels and Their Seasonality

The spectral unbiasing procedure presented in section 2.2 only impacts on the smallest resolvable scales (high wave number part of the spectrum). Our first analyses will focus on how the 1-Hz error levels associated with each altimeter vary spatially and temporally (Figure 3). Dufau et al. (2016) analyzed these error levels for Jason-2 and 7 months of Saral-AltiKa data. Here we analyze a longer 2-year Saral series and include an analysis of 10 months of Sentinel-3 SAR data.

In general, the three instruments exhibit similar spatial patterns, with the highest error levels concentrated at latitudes higher than 40°. This is consistent with the findings of Dufau et al. (2016), who observed the lowest error levels between 40°S and 40°N, and higher error levels in the high-latitude regions mainly related to the higher significant wave height conditions there (Zanife et al., 2003).

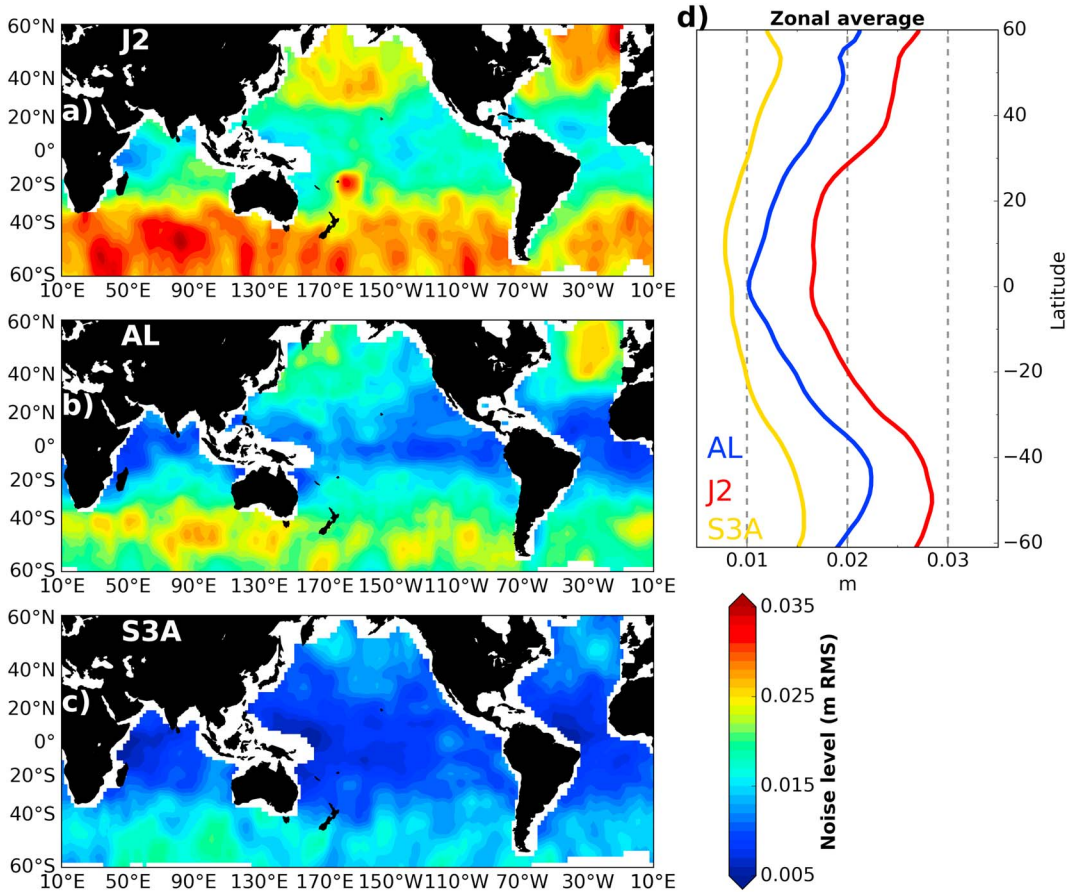

Figure 3. Global distribution of noise floors (in meter root mean square [RMS]) computed inside the spectral wavelength range 15-30 km for (a) Jason-2 (J2), (b) AltiKa (AL), and (c) Sentinel-3A (S3A). (d) Zonal average of the error levels plotted in left-hand panels.

In addition, we also observe the dramatic improvement in SSH error levels achieved by S3A, which is around 40% of the AltiKa error level (itself 30% lower than Jason-2) in the low to middle latitudes and reaches 50% (with respect to AltiKa) in the high latitudes (Figure 3d). The global Root Mean Square (RMS) mean error level for S3A is 1.12 cm, with 1.66 for AltiKa and 2.23 for Jason-2.

The SSH error levels also exhibit a conspicuous seasonal signal (Figure 4), with amplitudes that go from 1.8 cm RMS for Jason-2, 1.5 cm RMS in AltiKa, with the lowest error values always taking place during summer months (Figure 4). These results are consistent with Dufau et al. (2016), who report similar spatial patterns and amplitude of the seasonal cycle of the error levels, with increased winter noise levels related to higher wind/wave conditions in winter.

The main differences with the results reported in Dufau et al. (2016) occur in the northern hemisphere for AltiKa (error levels in our case tend to be slightly higher). This is likely to be related to the limited time period used in the previous work. In their case, Dufau et al. (2016) only used the first 7 months of the AltiKa (March–October 2013) mission in order to construct their diagnosis of both spectral slopes and error levels (as opposed to 24 months used in the present paper). Given that the lowest errors are observed during the summer months, the lack of the December-January-February months in their analysis led to an underestimation of the error levels in the northern hemisphere (bias toward NH summer months), and therefore, the amplitude of the average error levels would appear smaller than our estimations (Figure 3; Figure 7 in Dufau et al., 2016).

The seasonal changes in the SSH error levels strongly suggest a relation to local oceanic/atmospheric conditions such as significant wave height, rain cells, wind streaks, and ocean slicks (Bonnefond et al., 2018). In this regard, Dibarboure et al. (2014) showed that the inhomogeneities in the ocean surface, as well as

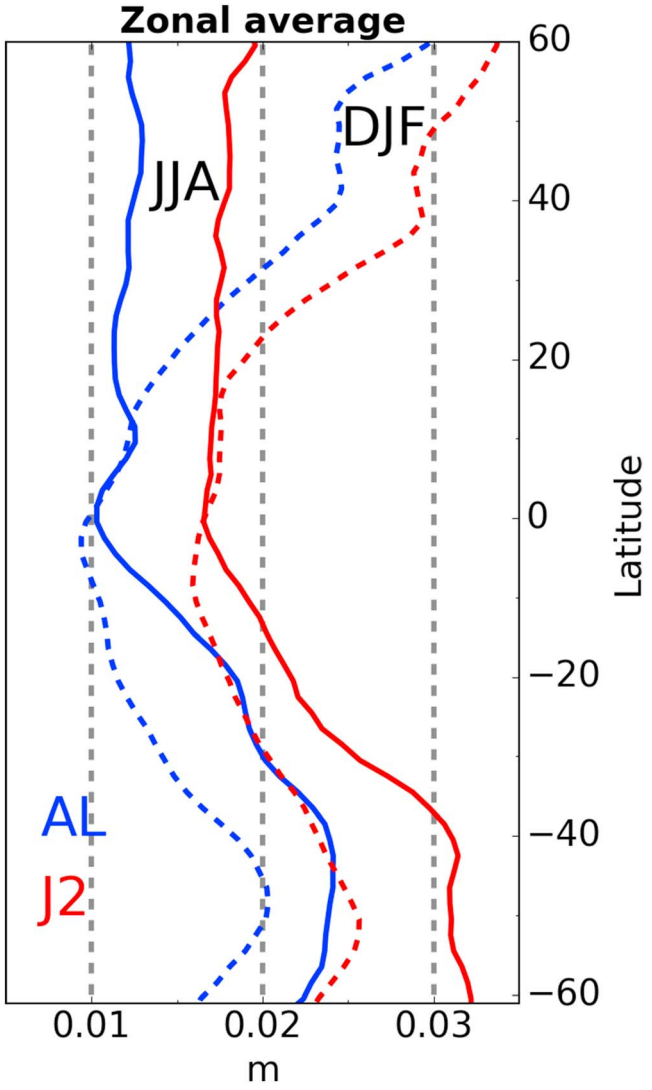

Figure 4. Zonal average of the seasonal variations (June-July-August [JJA] and December-January-February [DJF]) for the noise floors of AltiKa (AL) and Jason-2 (J2) depicted in Figure 3.

atmospheric events, constructively contribute to increase the error level in the SSH signal for wavelengths below 100 km ("hump" artifact, cf. Dibarboure et al., 2014) and particularly in the low-resolution data (i.e., the 1-Hz data used in the present paper). In that work the authors also contrasted the impact of this type of error for different classes of altimeters, namely, between Jason-class altimeters and the Cryosat-2 SAR altimeter (analog to S3A). This hump error was nonexistent in the SAR altimeter and contributes to the important difference in the error levels between Jason-2/AltiKa versus Sentinel-3A (Figure 3).

3.2. Average Spectral Slope

Once the variable error levels have been subtracted from the spectra, we analyze the unbiased spectral slopes in the mesoscale wavelength range, using the variable wavelength technique introduced in section 2.3.

The global distribution of SSH spectral slope estimates using the variable mesoscale wavelength range (hereafter SSH spectral slope) is consistent for the three satellites analyzed (Figure 5). There is general agreement with the spatial distribution reported in Xu and Fu (2011, 2012) and Dufau et al. (2016), although the values obtained using the current methodology are higher than the previously published results in the tropics and high latitudes (cf. section 2.3).

The highest values of the average spectral slope are observed in the midlatitude western boundary current systems (Kuroshio, Gulf Stream, Agulhas current, and the Brazil-Malvinas current) where slopes higher than $k^{-11/3}$ are observed and in the Antarctic Circumpolar Current (reaching k^{-5}, Figure 5), in agreement with SQG and QG theoretical predictions. Previously reported spectral slopes observed in the western boundary regions were slightly weaker, less than $k^{-11/3}$ (Dufau et al., 2016; Xu & Fu, 2012). Note that even in the highly energetic Gulf Stream region, we observe a slight increase in the spectral slope computed using our variable wavelength range (Figure 2c, box 3). We also observe that J2 has a consistently lower spectral slope than AL and S3 in the middle to high latitudes. This could be related to the fact that the noise level of J2 hides ocean variability out to ~70 km in wavelength, which is close to the eddy length scale used to fit the spectral slope (see Figure A1). Any error in the noise removal procedure could add energy in a wavelength band close to the eddy length scale used to compute the spectral slope and would result in a shallower slope. This agrees with the observations presented in Figure 5.

In contrast to the middle-to-high latitudes, the lowest slope values are located in the intertropical band (20°S–20°N) with SSH slope values around k^{-2}, and in the eastern boundary current systems (slope around k^{-3}). With respect to the low spectral slope values observed in the tropics, recent modeling studies (e.g., Qiu et al., 2018) find that in these regions the KE levels related to the geostrophically balanced motions (i.e., mesoscale eddies) would be lower than the KE levels due to nonbalanced motions (i.e., internal waves) and therefore the latter would mask the energy levels associated with mesoscale eddies (Savage, Arbic, Richman, et al., 2017; Tchilibou et al., 2018). This would explain the rather shallow spectral slopes observed by satellite altimetry at these latitudes, which are very close to the k^{-2} slope values predicted from the Garrett-Munk spectrum (Garrett & Munk, 1972). Our variable wavelength slope values (close to a k^{-2} power law) are calculated over longer wavelength bands from 180 up to 500 or 800 km (see Figure 2c) and include most of the long-wavelength tropical mesoscale energy (Tchilibou et al., 2018), leading to higher slope values than previously reported for the fixed wavelength range at low-latitude regions (less than 1). Adjusting the wavelength range for the spectral slope fitting in the present paper contributes to minimizing the impact of unbalanced smaller-scale motions.

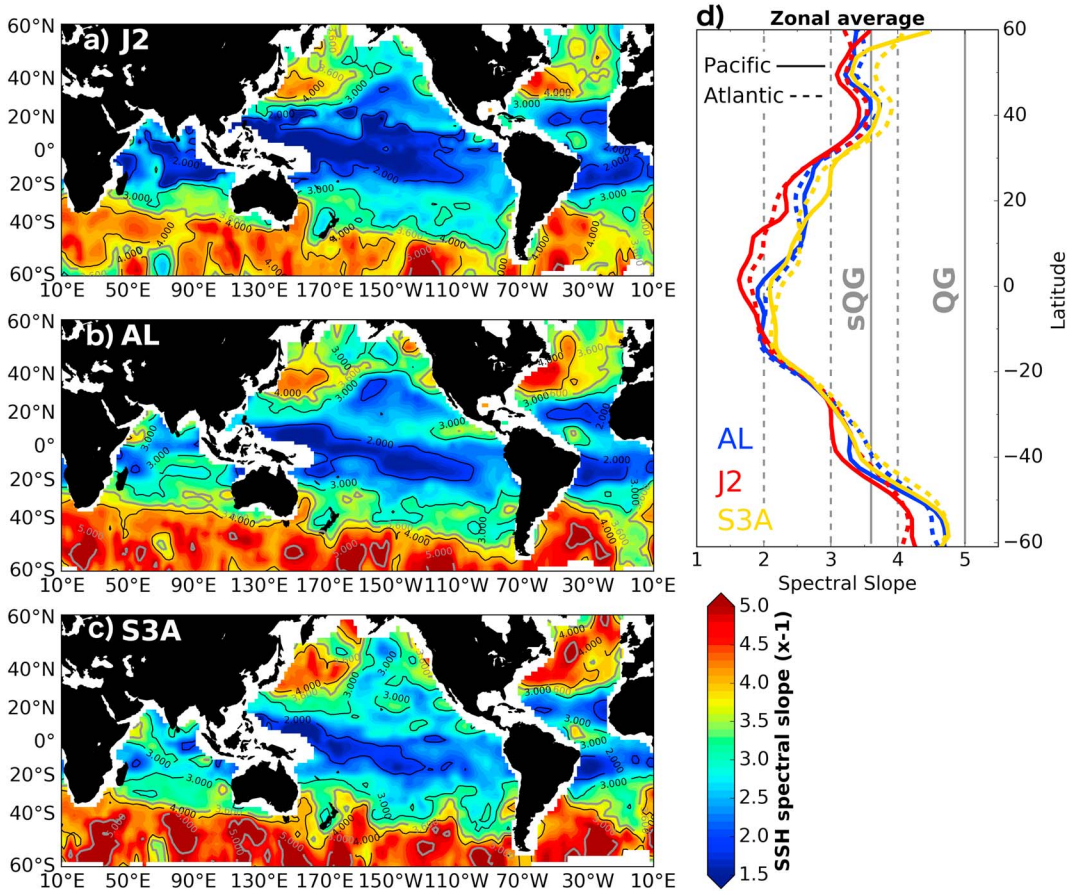

Figure 5. Global distribution of average spectral slope values (multiplied by -1) for Jason-2 (J2), AltiKa (AL), and Sentinel-3A (S3A). Zonal averages for the Pacific and Atlantic oceans are shown in the right-hand panel. Slope values of 11/3 (surface quasigeostrophic [SQG]) and 5 (quasigeostrophic [QG]) are also plotted as reference.

Part of the energy associated with nonbalanced motions in the tropics could come from the internal tide field (e.g., Dufau et al., 2016; Savage, Arbic, Richman, et al., 2017). The signal associated with the internal tide is only a few centimeters in amplitude in the SSH signal, and at spatial scales similar to the mesoscale structures, which makes them very difficult to extract from the along-track SSH measurements. Recently, Ray and Zaron (2016) proposed a phase-locked internal tide correction for the SSH signal, based on the dominant M2 tidal constituent, which could be applied to altimetry data. We have tested the impact of this new phase-locked correction on our spectral slope estimates. This SSH correction is computed following the methodology of Ray and Zaron (2016), and the main results of its application can be found in Zaron and Ray (2017).

Figure 6a illustrates the impact of the phase-locked internal tide correction on the spectral slope estimates for a region in the South Atlantic (spectral slope fitted in the wavelength range 110-330 km in Figure 6a). Here, energy peaks associated with the first and second modes of the internal tide signal appear to be located around 150- and 75-km wavelength, respectively (Figure 6a). Note that in the correction applied here, only the phase-locked internal tide is considered, and the weaker broad band remaining after applying the correction likely corresponds to non-phase-locked or incoherent internal tides.

Removing the phase-locked internal tide bump in this South Atlantic Region increases the slope from 1.8 to 2.5 for AL, and similar results are obtained for S3A (Figure 6a). Figures 6b and 6c show the geographical distribution of these slope changes, and we observe that the main effect concentrates in the midlatitudes of the Atlantic and Pacific Ocean, around the main internal tide generation and propagation sites (Zaron & Ray, 2017). Nevertheless, this result is only valid for the impact of phase-locked M2 internal tides on the SSH signal. There is a significant amount of SSH variability related to other tidal constituents, non-phase-locked internal tides, and the full IGW spectrum that is not accounted in the present comparison. These

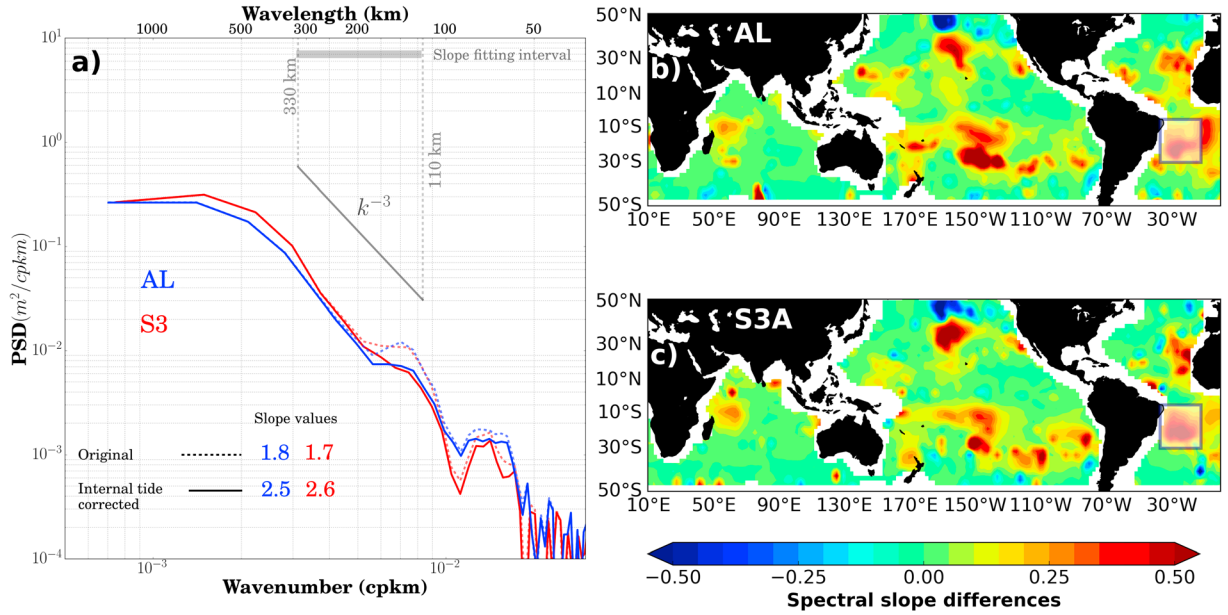

Figure 6. (a) Mean wave number spectra computed inside the highlighted region in (b) and (c), for AltiKa (AL), and Sentinel-3A (S3A). Slope corresponding to k^{-3} is plotted as reference. (b and c) Difference in spectral slope values obtained after applying the correction for coherent internal tides (corrected – not corrected). PSD = power spectral density.

unbalanced processes could have a similar impact on the spectral slope values as observed here (i.e., inducing shallow spectral slope values).

3.3. Spectral Slope Seasonality

Figures 7a and 7b show the global pattern of spectral slope values for summer and winter observed in the AltiKa and J2 SSH series, both exhibiting a similar spatial pattern, and Figure 7e shows a summary of the seasonal differences for AltiKa.

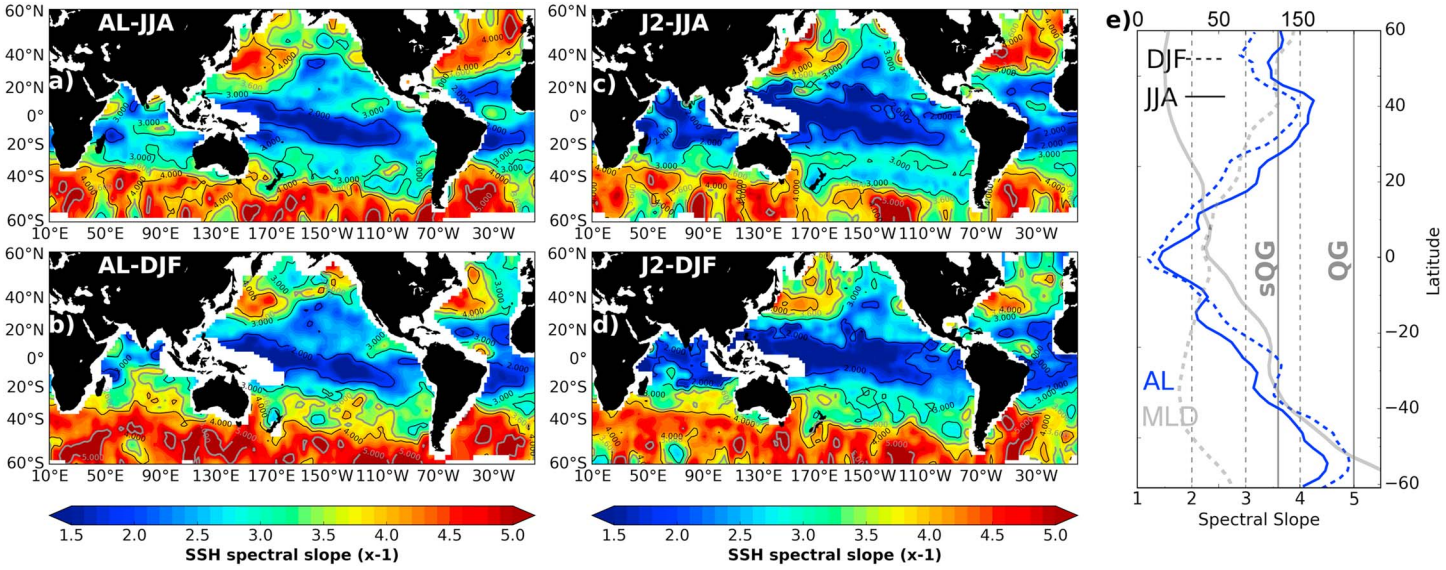

Figure 7. Seasonal sea surface height (SSH) spectral slope values for (a and b) AltiKa (AL) and (c and d) Jason-2 (J2), computed over the months June-July-August (JJA) and December-January-February (DJF). (e) Zonal average of the SSH spectral slope values over the Atlantic Ocean for AL. Slope values of 11/3 (surface quasigeostrophic [SQG]) and 5 (quasigeostrophic [QG]) are also plotted as reference values. Climatological mixed layer depth (MLD) values over the Atlantic Ocean for JJA (solid) and DJF (dashed) are also plotted (gray shading lines). Note the different ranges used to plot the MLD values from 0- to 200-m depth (top), and SSH spectral slope values from 1 to 5 (bottom).

In general, shallower spectral slope values are found during winter compared to summer. This difference is particularly strong in the highly energetic regions (western boundary currents and Antartic Circumpolar current). The seasonal changes in the spectral slope values are in the order of 20% for the western boundary currents, 10% for the eastern boundary currents, and 15% for the ACC, always exhibiting steeper spectral slopes during summer in compared to winter.

We observe that there is a local regime change from summer to winter, which is particularly noticeable in the midlatitude western boundary currents (in both hemispheres). During summer months the spectral slope values are close to QG predictions (k^{-4} to k^{-5}). On the other hand, the spectral slope values during winter months are close to a SQG-type regime (k^{-3} to k^{-4}). This summer/winter spectral slope asymmetry is also evidenced in the zonally averaged analysis for the Atlantic Ocean (Figure 7e), despite the fact that contrasting dynamical current systems are being considered in this result (eastern/western boundary currents systems).

The seasonal variability in the spectral slope values observed here is consistent with the seasonal modulation of the ocean dynamics by the atmosphere and the impact of oceanic multiscale interactions at mesoscale and submesoscale, as reported, for example, in the Northern Pacific Ocean (Qiu et al., 2014; Sasaki et al., 2014), in Drake Passage (Rocha, Gille, et al., 2016), or in the Atlantic Ocean (Callies & Ferrari, 2013). Observational and modeling evidence suggests that such seasonal changes emerge essentially from the mixed layer depth seasonality. Figure 7e also indicates the climatological mixed layer depth values for summer and winter (de Boyer Montégut et al., 2004).

During summer, the presence of a thin mixed layer with a strong pycnocline at its base works to trap and enhance the surface unbalanced motions KE for wavelengths shorter than 100 km (Rocha, Chereskin, et al., 2016). Conversely, the deepening of the mixed layer that takes place during winter (closely related to atmospheric control) favors the development of mixed layer instabilities, exhibiting vigorous vertical motions with small scales and large amplitudes (Boccaletti et al., 2007; Sasaki et al., 2014). Furthermore, mixed layer instabilities would favor the development of frontal instabilities in the O(1-50 km) wavelength range (Stone, 1966) during the winter. It is unlikely we would observe these scales given the noise levels of the three altimeters used in this study. However, modeling shows that the KE growth that takes place at small wavelengths during winter feeds energy into the mesoscale wavelength range through an inverse energy cascade, starting the end of the winter (e.g., in the Northern Pacific 70% of KE flux at 200 km in winter is explained by the contributions of scales smaller than 100 km; see Sasaki et al., 2014). We could then expect that the energy levels of the balanced motions in the mesoscale wavelength range would overcome those of the unbalanced motions by the end of the winter. This interpretation is consistent with the SSH spectral slope values observed in Figure 7, with wintertime spectral slopes being flatter (more small-scale SSH variability) than those observed during summer for the three satellites, related to the increase in energy levels in the mesoscale wavelength range. Due to the lower noise levels of recent altimeters such as AltiKa, we are now capable of observing these small-scale instabilities, previously revealed in models.

4. Discussion and Conclusions

In this paper we have revisited the estimates of SSH spectral slope in the mesoscale wavelength range using observations from three different altimeters: Jason-2 and AltiKa (2013-2015) and the first 10 months of the Sentinel-3A mission. The first modification compared to previous works on the same subject (e.g., Xu and Fu (2012), Dufau et al. (2016)) is to no longer use a fixed "mesoscale" wavelength range across the ocean. Rather, we use a variable wavelength range based on dynamical (following Eden (2007)) and empirical considerations (as a function of the spectrum itself; cf. Appendix A) that have a local dependency. Indeed, the size of the mesoscale structures is highly dependent on the local Rossby radius of deformation and stratification (Jacobs et al., 2001; Le Traon et al., 1990), which will be reflected in the shape of local SSH spectra. The main benefit of this approach is that we generally obtain higher values of spectral slopes in the mesoscale wavelength range in comparison to previous studies, particularly in the energetic midlatitude regions, high latitudes, and the tropics.

Similarly to Dufau et al. (2016) and Xu and Fu (2011), we observe low spectral slope values in the intertropical band and the low-energy eastern basins. In these low-energy regions it is not possible to distinguish between the geostrophically balanced motions (viz., mesoscale turbulence) and the unbalanced motions (i.e., IGWs), which are in turn characterized by a relatively shallow slope (around k^{-2}; Garrett and Munk

(1972)). Note that the unbalanced motions have a k^{-2} spectral slope in both SSH and KE. This issue becomes important where the energy due to the unbalanced motions is higher than that associated with geostrophic turbulence, as has been reported in the tropics (e.g., Qiu et al., 2018). So, even though the variable wavelengths resolved in this region are above the local eddy length scale and the local noise level (cf. Figure A1), we are still fitting a curve to a statistical combination of the signals of balanced and unbalanced motions, since the latter can extend out to wavelengths greater than 200 km in the tropics (Tchilibou et al., 2018). In contrast, as we approach regions with more energetic mesoscale structures (high latitudes and western boundary current systems), we observe spectral slopes closer to QG predictions (k^{-4} to k^{-5}). Less energetic regions such as the eastern boundary current systems exhibit in turn spectral slopes smaller than k^{-3}, with more influence from unbalanced motions (Qiu et al., 2018; Richman et al., 2012).

The zonal average across the midlatitudes is closer to SQG theory (Figure 5), but this is a computational result of averaging across k^{-5} and k^{-3} regions. As noted by Xu and Fu (2012), the geographical area with mean $k^{-11/3}$ slopes is quite small at midlatitudes. Please note that the zonal averages depicted in Figure 5 as a reference for spectral slope values might encompass contrasting dynamical regions. Therefore, they must be interpreted with caution.

These multiyear mean slope values also mask the distinct seasonality of the spectral slope values observed here, which are consistent with the most recent interpretations of the dynamics in the mesomesoscale to submesoscale wavelength range (Qiu et al., 2017, 2018 ; Sasaki et al., 2014). However, due to the methodology adopted in the present paper, the amplitude of the seasonal cycle of spectral slope values could be underestimated. In the computation of the Rhines scale used to calculate the Eddy transition scale as defined by Eden (2007; cf. Appendix A), we use the time mean Eddy Kinetic Energy (EKE) field as a proxy for the currents variability, instead of a seasonally varying one. Although this could impact the value of Eddy length scale obtained, its effect would be in O(10 km), which is minor compared to the reported seasonality in the mesoscale to submesoscale transition scale (Qiu et al., 2018).

An additional source of uncertainties could come from our estimations of the altimeter noise level. In the present paper we use a similar methodology to previous studies (i.e., we assume a white noise between 15 and 30 km), and we use 1-Hz SSH measurements despite the fact that higher-resolution along-track SSH products are also available. Using the 1-Hz data allows us to directly compare our results with previous works that adopted a similar approach.

The J2 20-Hz spectra have a lower noise floor from 350-m to 7-km wavelength, and a spectral hump from 3- to 10-km wavelength related to surface conditions and the altimeter waveform processing. It is possible that using 20-Hz SSH measurements instead of 1 Hz would help to minimize the impact of the hump artifact on the observed spectral shape for wavelengths larger than 70 km, as reported by Dibarboure et al. (2014). However, these authors demonstrate that the hump PSD consistently exhibits a flat plateau between 10 and 50 km, when considering several along-track segments of at least 1,000-km length. This means that using a relatively long time series of long along-track segments would ensure that the error in considering the hump plateau as a flat spectrum is negligible, thus validating the methodology used in the present paper for this type of error.

The interpretation of the 1-Hz S3A data is more complicated. Although S3A has no hump artifact in its PSD, the SSH measurements from this mission are characterized by a red-colored noise below 70 km (Raynal et al., 2017). In denoising the S3A spectra, we have applied a red noise fit (i.e., not flat) calculated in the 15- to 30-km wavelength range, then extended this over wavelengths larger than 30 km. Due to the "red" characteristic of S31 noise level in the 15-30 km, the energy level removed from the SSH spectrum is not uniform across the entire wavelength range. This means that the energy level subtracted will be larger at small wave numbers (i.e., overestimation of the error level for small wave numbers).

Any overestimation of the instrument error, once subtracted, could potentially induce an underestimation of the spectral slope values. This straight line "red" slope also assumes no curvature in the spectrum. Despite this sensitivity, the spectral estimates obtained from 1-Hz S3A SSH along-track data are consistent with the other altimetric data sets (Figure 5), suggesting that S3 instrument slope error estimate is reasonable. In addition, the lower noise levels obtained for S3A in comparison to Jason-2 and AltiKa imply that we can observe more SSH variability in the shallow mesoscale wavelength range, which has been difficult

using the current generation of altimeters. A reprocessing of the S3A data is being carried out by the French Space Agency (Boy et al., 2017), and tests show they may have solved the issue of the red-colored noise. In the future, this should allow us to exploit the full capabilities of the global SAR coverage provided by this mission.

This is directly related to one of the challenges for the future SWOT mission. As has been recently shown by observational (Qiu et al., 2017; Rocha, Chereskin, et al., 2016; Rocha, Gille, et al., 2016) and modeling studies (Qiu et al., 2018; Sasaki et al., 2014), the mesoscale to submesoscale spectral region is difficult to interpret from altimetry due to the inability to disentangle the geostrophically balanced motions from its unbalanced counterpart using high-resolution along-track data. SWOT will provide unique 2-D observations of their combined SSH signal over even smaller scales down to 15 to 30 km, depending on wave conditions (due to SWOT's lower noise; Morrow et al., 2018). In the meantime, we can only document the mesoscale to submesoscale region of the spectrum using the current generation 1-D altimeters. The characterization of the variable mesoscale wavelength range and a distinct IGW spectral slope is part of our ongoing efforts using currently available SSH data.

Appendix A: Eddy Spatial Scales for Spectral Slope Estimations

Spectral slope values reported in the literature using altimetric SSH have been consistently lower than what is expected from QG and SQG theories. In the present paper we revisit the methodology used to compute the spectral slope values in order to tackle this discrepancy between observations and theory. Instead of using a constant "mesoscale wavelength range" from 70 to 250 km in wavelength to compute the spectral slopes across the global ocean (e.g., Dufau et al., 2016; Xu & Fu, 2011), we build our definition on a dynamical criteria related to the local ocean characteristics, and to the local SSH spectrum itself. The lower limit of the wavelength range used to compute the slopes is therefore defined by the local eddy length scale (Eden, 2007), whereas the upper limit is imposed by the change of the spectrum shape, that is, the change in slope itself. These limits are denoted by the black arrows at the bottom of Figure 1a and are determined for this particular region (Figure 1b).

The local eddy length scale is used as a proxy for the characteristic spatial scale of mesoscale turbulence and is estimated following Eden (2007) as the minimum value between the local first Rossby radius of deformation (L_r) and the local Rhines scale (L_R). The spatial distribution of the eddy length scale computed in this manner is presented in Figure A1a. We observe the highest values in the tropical band (15°S–15°N), related to the fact that the turbulent flow is characterized in this region as being zonally elongated (anisotropic),

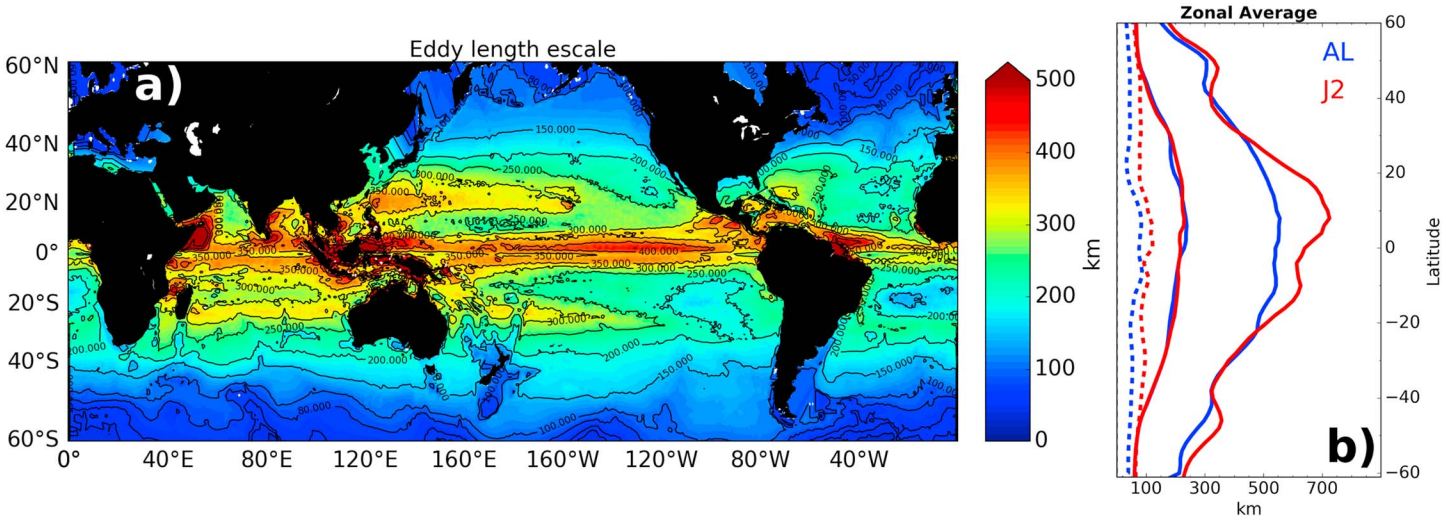

Figure A1. (a) Spatial distribution of the eddy length scale used as the lower limit for the spectral slope computation. (b) Zonal average of the lower and upper limits (full line) of the wavelength range used to fit the spectral slope for AltiKa (AL) and Jason-2 (J2). Dashed lines correspond to the effective resolution (spectral signal to noise ratio equal to 1) for AL and J2.

while it becomes progressively isotropic toward the poles, hence the decrease in eddy length scale. Figure A1b shows the zonal average of the lower bounds of our variable wavelength range based on the local eddy length scale for AltiKa and Jason-2 (first full line from the left) and the upper bounds based on the change in spectral slope (second full line from the left). The effective resolution above the noise level (30 km) is also plotted (dashed line), illustrating the fact that the spectral slope fit falls outside of the region where the signal-to-noise ratio is less than one.

Please note that geostrophically balanced motions might exist at spatial scales smaller than the wavelength range defined using the present methodology (Qiu et al., 2017; Rocha, Chereskin, et al., 2016; Rocha, Gille, et al., 2016). Nevertheless, we decided to limit the wavelength range using the local eddy length scale in order to overcome the inherent difficulties of the observations used. SSH measurements from satellite altimetry contain a combination of both geostrophically balanced and unbalanced motions, which are, for the time being, impossible to disentangle using 1-D SSH data only. They also contain measurement noise affecting scales out to 30-70 km if uncorrected. In using the local eddy length scale as a proxy for the local size of the mesoscale turbulence, we aim to focus on the larger "balanced" part of the energy spectrum (i.e., the wavelength range that is dominated by mesoscale turbulence). Therefore, by using the eddy scale as the lower limit, we ensure that the spectral slope estimates are computed over a wavelength range that is essentially dominated by geostrophically balanced motions.

We follow a similar methodology as the one used in Eden (2007) to evaluate the skill of the eddy length scale as a metric for the local mesoscale turbulence spatial scale, obtaining analog results to what is reported in

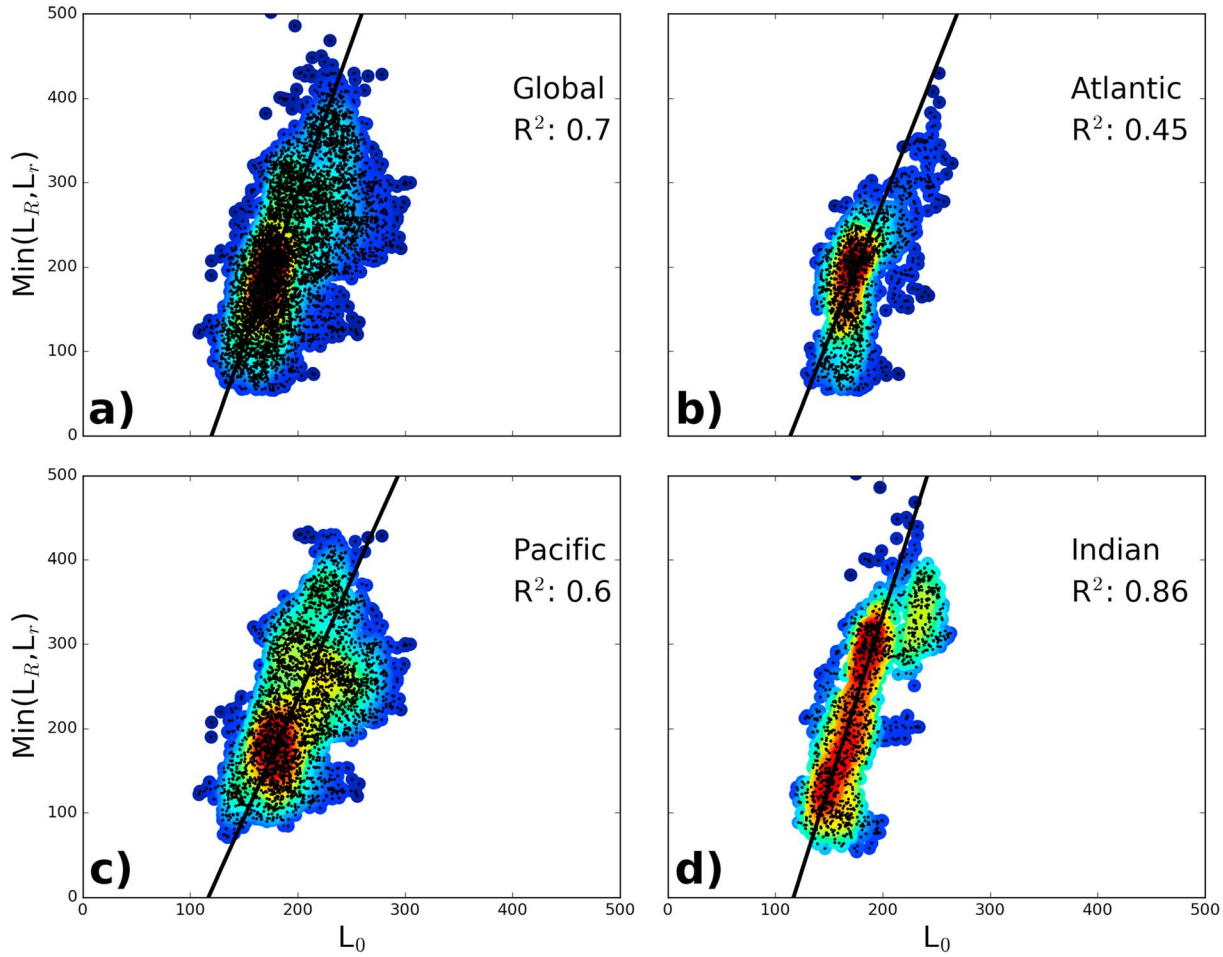

Figure A2. Eddy length scale (y axis) versus length scale (L_0) calculated from AltiKa along-track data, averaged over the global ocean (a), and for the Atlantic (b), Pacific (c), and Indian (d) basins. Time period corresponds to 2013-2015. Color shading denotes the point density (warm colors equals high point density). Units in kilometers. Solid black lines denote the regression of L_0 over the eddy length scale (regression coefficient R^2 is also indicated).

that work for the North Atlantic. One of the metrics often used to characterize the eddy length scales is the first zero crossing of the autocovariance function, L_0 (Stammer, 1997), which shows a rapid decay with increasing spatial lags. One disadvantage of this metric is that the result will depend on the altimeter measurement itself and therefore would be subject to the precision of the along-track data. Nevertheless, we have compared our estimations of eddy length scale to L_0 values observed by AltiKa, as a way of verifying the skill of the eddy length scale in representing the characteristic spatial scales of mesoscale turbulence. Figure A2 plots the dispersion diagrams of the local eddy length scale versus the spatial scale L_0 and shows a good agreement between the two metrics, suggesting that the eddy length scale can indeed be used as an independent metric that locally characterizes the spatial scale of mesoscale turbulence.

Acknowledgments
The Jason-2, SARAL/AltiKa and Sentinel-3A data were computed from the Geophysical Data Record (GDR) available on the AVISO website (https://www.aviso.altimetry.fr). The Mean Sea Surface Model CNES_CLS_2015 is also available on the same website. Mixed Layer Depth data are available at the IFREMER MLD climatology website (http://www.ifremer.fr/cerweb/deboyer/mld/home.php). The authors would like to acknowledge the support from the French Space Agency (CNES) received to conduct the present study. The authors would like to thank the two anonymous reviewers for their comments that helped improving the original manuscript.

References

Andersen, O. B., Cheng, Y., & Knudsen, P. (2016). A new 25 years Arctic Sea level record from ESA satellites. Paper presented at ESA Living Planet Symposium 2016, Prague, Czech Republic.

Blumen, W. (1978). Uniform potential vorticity flow: Part I. Theory of wave interactions and two-dimensional turbulence. *Journal of Atmospheric Sciences*, *35*(5), 774–783. https://doi.org/10.1175/1520-0469(1978)035<0774:UPVFPI>2.0.CO;2

Boccaletti, G., Ferrari, R., & Fox-Kemper, B. (2007). Mixed layer instabilities and restratification. *Journal of Physical Oceanography*, *37*(9), 2228–2250. https://doi.org/10.1175/JPO3101.1

Bonnefond, P., Verron, J., Aublanc, J., Babu, K. N., Bergé-Nguyen, M., Cancet, M., et al. (2018). The benefits of the Ka-Band as evidenced from the SARAL/AltiKa Altimetric Mission: Quality assessment and unique characteristics of AltiKa data. *Remote Sensing*, *10*(2). https://doi.org/10.3390/rs10010083

Boy, F., Moreau, T., Thibaut, P., Rieu, P., Aublanc, J., Picot, N., et al. (2017). New stacking method for removing the SAR sensitivity to swell. Paper presented at Ocean Topography Science Team (OSTST) meeting 2017, Miami FL, United States of America.

Brannigan, L., Marshall, D. P., Naveria-Garabato, A., & Nurser, A. J. (2015). The seasonal cycle of submesoscale flows. *Ocean Modelling*, *92*, 69–84. https://doi.org/10.1016/j.ocemod.2015.05.002

Callies, J., & Ferrari, R. (2013). Interpreting energy and tracer spectra of upper-ocean turbulence. *Journal of Physical Oceanography*, *43*(11), 2456–2474. https://doi.org/10.1175/JPO-D-13-063.1

Callies, J., Ferrari, R., Klymak, J. M., & Gula, J. (2015). Seasonality in submesoscale turbulence. *Nature Communications*, *6*(1), 6862. https://doi.org/10.1038/ncomms7862

Charney, J. G. (1971). Geostrophic turbulence. *Journal of the Atmospheric Sciences*, *28*(6), 1087–1095. https://doi.org/10.1175/1520-0469(1971)028<1087:GT>2.0.CO;2

Cotton, P. D., Andersen, O. B., Stenseng, L., Boy, F., Cancet, M., Cipollini, P., et al. (2016). Improved oceanographic measurements from SAR altimetry: Results and scientific roadmap from ESA cryosat plus for oceans project. Paper presented at ESA Living Planet Symposium 2016, Prague, Czech Republic.

de Boyer Montégut, C., Madec, G., Fischer, A. S., Lazar, A., & Iudicone, D. (2004). Mixed layer depth over the global ocean: an examination of profile data and a profile-based climatology. *Journal of Geophysical Research*, *109*, C12003. https://doi.org/10.1029/2004JC002378

Dibarboure, G., Boy, F., Desjonqueres, J. D., Labroue, S., Lasne, Y., Picot, N., et al. (2014). Investigating short-wavelength correlated errors on low-resolution mode altimetry. *Journal of Atmospheric and Oceanic Technology*, *31*(6), 1337–1362. https://doi.org/10.1175/JTECH-D-13-00081.1

Dufau, C., Orsztynowicz, M., Dibarboure, G., Morrow, R., & Le Traon, P.-Y. (2016). Mesoscale resolution capability of altimetry: Present and future. *Journal of Geophysical Research: Oceans*, *121*, 4910–4927. https://doi.org/10.1002/2015JC010904

Eden, C. (2007). Eddy length scales in the North Atlantic Ocean. *Journal of Geophysical Research*, *112*, C06004. https://doi.org/10.1029/2006JC003901

Fu, L.-L. (1983). On the wavenumber spectrum of oceanic mesoscale variability observed by the Seasat altimeter. *Journal of Geophysical Research*, *88*(C7), 4331–4341. https://doi.org/10.1029/JC088iC07p04331

Garrett, C. J. R., & Munk, W. H. (1972). Space-time scales of internal waves. *Geophysical Fluid Dynamics*, *80*(3), 291–297. https://doi.org/10.1029/JC080i003p00291

Held, I. M., Pierrehumbert, R. T., Garner, S. T., & Swanson, K. L. (1995). Surface quasi-geostrophic dynamics. *Journal of Fluid Mechanics*, *282*(1), 1–20. https://doi.org/10.1017/S0022112095000012

Hosoda, K., Kawamura, H., & Sakaida, F. (2015). Improvement of New Generation Sea Surface Temperature for Open ocean (NGSST-O): A new sub-sampling method of blending microwave observations. *Journal of Oceanography*, *71*(2), 205–220. https://doi.org/10.1007/s10872-015-0272-x

Jacobs, G. A., Barron, C. N., & Rhodes, R. C. (2001). Mesoscale characteristics. *Journal of Geophysical Research*, *106*(C9), 19,581–19,595. https://doi.org/10.1029/2000JC000669

Lambin, J., Morrow, R., Fu, L.-L., Willis, J., Bonekamp, H., Lillibridge, J., et al. (2010). The OSTM/Jason-2 Mission. *Marine Geodesy*, *33*(sup1), 4–25. https://doi.org/10.1080/01490419.2010.491030

Le Traon, P. Y., Klein, P., Hua, B. L., & Dibarboure, G. (2008). Do altimeter wavenumber spectra agree with the interior or surface quasi-geostrophic theory? *Journal of Physical Oceanography*, *38*(5), 1137–1142. https://doi.org/10.1175/2007JPO3806.1

Le Traon, P. Y., Rouquet, M. C., & Boissier, C. (1990). Spatial scales of mesoscale variability in the North Atlantic as deduced from GEOSAT data. *Journal of Geophysical Research*, *95*(C11), 20,267–20,285. https://doi.org/10.1029/JC095iC11p20267

Morrow, R., Blumstein, D., & Dibarboure, G. (2018). Fine-scale altimetry and the future SWOT Mission. In E. Chassignet, A. Pascual, J. Tintoré, & J. Verron (Eds.), *New Frontiers in Operational Oceanography, GODAE OceanView* (pp. 191–226). CreateSpace Independent Publishing Platform. https://doi.org/10.17125/gov2018

Morrow, R., Carret, A., Birol, F., Nino, F., Valladeau, G., Boy, F., et al. (2017). Observability of fine-scale ocean dynamics in the Northwestern Mediterranean Sea. *Ocean Science*, *13*(1), 13–29. https://doi.org/10.5194/os-13-13-2017

Pujol, M.-I., Schaeffer, P., Faugère, Y., Raynal, M., Dibarboure, G., & Picot, N. (2018). Gauging the improvement of recent mean sea surface models: A new approach for identifying and quantifying their errors. *Journal of Geophysical Research: Oceans*, *123*, 5889–5911. https://doi.org/10.1029/2017JC013503

Qiu, B., Chen, S., Klein, P., Sasaki, H., & Sasai, Y. (2014). Seasonal mesoscale and submesoscale eddy variability along the North Pacific Subtropical Countercurrent. *Journal of Physical Oceanography*, *44*(12), 3079–3098. https://doi.org/10.1175/JPO-D-14-0071.1

Qiu, B., Chen, S., Klein, P., Wang, J., Torres, H., Fu, L.-L., & Menemenlis, D. (2018). Seasonality in transition scale from balanced to unbalanced motions in the world ocean. *Journal of Physical Oceanography*, *48*(3), 591–605. https://doi.org/10.1175/JPO-D-17-0169.1

Qiu, B., Nakano, T., Chen, S., & Klein, P. (2017). Submesoscale transition from geostrophic flows to internal waves in the northwestern Pacific upper ocean. *Nature Communications*, *8*, 14055. https://doi.org/10.1038/ncomms14055

Ray, R. D., & Zaron, E. D. (2016). M2 internal tides and their observed wavenumber spectra from satellite altimetry. *Journal of Physical Oceanography*, *46*, 3–22. https://doi.org/10.1175/JPO-D-15-0065.1

Raynal, M., Labroue, S., Urien, S., Amarouche, L., Moreau, T., Boy, F., et al. (2017). Performances and assessment of Cryosat-2 and Sentinel-3A SARM over ocean inferred from existing ground processing chains. Paper presented at Ocean Surface Topography Science Team Meeting (OSTST) 2017, Miami FL, United States of America.

Richman, J. G., Arbic, B. K., Shriver, J. F., Metzger, E. J., & Wallcraft, A. J. (2012). Inferring dynamics from the wavenumber spectra of an eddying global ocean model with embedded tides. *Journal of Geophysical Research*, *117*, C12012. https://doi.org/10.1029/2012JC008364

Rocha, C. B., Chereskin, T. K., Gille, S. T., & Menemenlis, D. (2016). Mesoscale to submesoscale wavenumber spectra in Drake Passage. *Journal of Physical Oceanography*, *46*(2), 601–620. https://doi.org/10.1175/JPO-D-15-0087.1

Rocha, C. B., Gille, S. T., Chereskin, T. K., & Menemenlis, D. (2016). Seasonality of submesoscale dynamics in the Kuroshio Extension. *Geophysical Research Letters*, *43*, 11,304–11,311. https://doi.org/10.1002/2016GL071349

Sasaki, H., Klein, P., Qiu, B., & Sasai, Y. (2014). Impact of oceanic-scale interactions on the seasonal modulation of ocean dynamics by the atmosphere. *Nature Communications*, *5*(1), 5636. https://doi.org/10.1038/ncomms5636

Savage, A. C., Arbic, B. K., Alford, M. H., Ansong, J. K., Farrar, J. T., Menemenlis, D., et al. (2017). Spectral decomposition of internal gravity wave sea surface height in global models. *Journal of Geophysical Research: Oceans*, *122*, 7803–7821. https://doi.org/10.1002/2017JC013009

Savage, A. C., Arbic, B. K., Richman, J. G., Shriver, J. F., Alford, M. H., Buijsman, M. C., et al. (2017). Frequency content of sea surface height variability from internal gravity waves to mesoscale eddies. *Journal of Geophysical Research: Oceans*, *122*, 2519–2538. https://doi.org/10.1002/2016JC012331

Schaeffer, P., Faugere, Y., Pujol, M.-I., Guillot, A., & Picot, N. (2016). The CNES CLS 2015 Global Mean Sea surface. Paper presented at Ocean Surface Topography Science Team Meeting (OSTST) 2016, La Rochelle, France.

Stammer, D. (1997). Global characteristics of ocean variability estimated from regional TOPEX/POSEIDON altimeter measurements. *Journal of Physical Oceanography*, *27*(8), 1743–1769. https://doi.org/10.1175/1520-0485(1997)027<1743:GCOOVE>2.0.CO;2

Stone, P. H. (1966). On Non-Geostrophic Baroclinic Stability. *Journal of the Atmospheric Sciences*, *23*(4), 390–400. https://doi.org/10.1175/1520-0469(1966)023<0390:ONGBS>2.0.CO;2

Tchilibou, M., Gourdeau, L., Morrow, R., Serazin, G., Djath, B., & Lyard, F. (2018). Spectral signatures of the tropical Pacific dynamics from model and altimetry: A focus on the meso/submesoscale range. *Ocean Science*, *14*(5), 1283–1301. https://doi.org/10.5194/os-14-1283-2018

Verron, J., Sengenes, P., Lambin, J., Noubel, J., Steunou, N., Guillot, A., et al. (2015). The SARAL/AltiKa Altimetry Satellite Mission. *Marine Geodesy*, *38*(sup1), 2–21. https://doi.org/10.1080/01490419.2014.1000471

Wortham, C., & Wunsch, C. (2013). A multidimensional spectral description of ocean variability. *Journal of Physical Oceanography*, *44*(3), 944–966. https://doi.org/10.1175/JPO-D-13-0113.1

Xu, Y., & Fu, L.-L. (2011). Global variability of the wavenumber spectrum of oceanic mesoscale turbulence. *Journal of Physical Oceanography*, *41*(4), 802–809. https://doi.org/10.1175/2010JPO4558.1

Xu, Y., & Fu, L.-L. (2012). The effects of altimeter instrument noise on the estimation of the wavenumber spectrum of sea surface height. *Journal of Physical Oceanography*, *42*, 2229–2233. https://doi.org/10.1175/JPO-D-12-0106.1

Zanife, O. Z., Vincent, P., Amarouche, L., Dumont, J. P., Thibaut, P., & Labroue, S. (2003). Comparison of the Ku-Band range noise level and the relative sea-state bias of the Jason-1, TOPEX, and Poseidon-1 radar altimeters. *Marine Geodesy*, *26*(3-4), 201–238. https://doi.org/10.1080/714044519

Zaron, E. D., & Ray, R. D. (2017). Using an altimeter-derived internal tide model to remove tides from in situ data. *Geophysical Research Letters*, *44*, 4241–4245. https://doi.org/10.1002/2017GL072950

Zhou, X.-H., Wang, D.-P., & Chen, D. (2015). Global wavenumber spectrum with corrections for altimeter high-frequency noise. *Journal of Physical Oceanography*, *45*(2), 495–503. https://doi.org/10.1175/JPO-D-14-0144.1